



# Open Access Articles

## ***Ocean Speed and Turbulence Measurements Using Pitot-Static Tubes on Moorings***

The Faculty of Oregon State University has made this article openly available.  
Please share how this access benefits you. Your story matters.

<b>Citation</b>	Moum, J. N. (2015). Ocean speed and turbulence measurements using pitot-static tubes on moorings. <i>Journal of Atmospheric and Oceanic Technology</i> , 32(7), 1400-1413. doi:10.1175/JTECH-D-14-00158.1
<b>DOI</b>	10.1175/JTECH-D-14-00158.1
<b>Publisher</b>	American Meteorological Society
<b>Version</b>	Version of Record
<b>Terms of Use</b>	<a href="http://cdss.library.oregonstate.edu/sa-termsofuse">http://cdss.library.oregonstate.edu/sa-termsofuse</a>

# Ocean Speed and Turbulence Measurements Using Pitot-Static Tubes on Moorings

JAMES N. MOUM

*College of Earth, Ocean, and Atmospheric Sciences, Oregon State University, Corvallis, Oregon*

(Manuscript received 14 August 2014, in final form 10 April 2015)

## ABSTRACT

A low-power ( $<10$  mW), physically small (15.6 cm long  $\times$  3.2 cm diameter), lightweight (600 g Cu; alternatively, 200 g Al), robust, and simply calibrated pitot-static tube to measure mean speed and turbulence dissipation ( $\varepsilon$ ) is described and evaluated. The measurement of speed is derived from differential pressure via Bernoulli's principle. The differential pressure sensor employed here has relatively small, but significant, adverse sensitivities to static pressure, temperature, and acceleration, which are characterized in tests in the college's laboratory. Results from field tests on moorings indicate acceptable agreement in pitot-static speed measurements with independent acoustic Doppler current profiler speeds, characterized as linear fits with slope = 1 (95% confidence),  $\pm 0.02$  m s $^{-1}$  bias, and root-mean-square error of residuals (observed minus fitted values) =  $0.055$  m s $^{-1}$ . Direct estimates of  $\varepsilon$  are derived from fits of velocity spectra to a theoretical turbulence inertial subrange. From near-bottom measurements, these estimates are interpreted as seafloor friction velocities, which yield drag coefficients consistent with expected values. Noise levels for  $\varepsilon$ , based on 40-min spectral fits, are  $<10^{-9}$  m $^2$  s $^{-3}$ . In comparison to the airfoil (or shear) probe, the pitot-static tube provides the full spectrum of velocity, not just the dissipation range of the spectrum. In comparison to acoustic measurements of velocity, the pitot-static tube does not require acoustic scatters in the measurement volume. This makes the sensor a candidate for use in the deep ocean, for example, where acoustic scatterers are weak.

## 1. Introduction

A pitot tube, or pitot-static tube, is a simple and commonly used device to determine velocity from a pressure measurement via Bernoulli's principle. These devices are found in industrial applications to measure flow speeds in pipes, for example, and on aircraft to provide a measure of airspeed. In most of these cases, ambient (or static) pressure is relatively small compared to those typically encountered in oceanographic applications. Consequently, device sensitivity to static pressure changes does not contribute a significant adverse effect to the measurement of flow speed, although temperature compensation may be needed. In our group, we have used pitot tubes on our vertical profiler, Chameleon, to determine velocity fluctuations about a mean speed (Moum 1990b,a) from which direct covariance flux estimates were made from profiling measurements (Moum 1996a) and inferences about the

energy-containing scales of thermocline turbulence (Moum 1996b). However, inherent device drift that was not well characterized precluded estimation of mean speed from these measurements.

More recently, we have been developing instrumentation ( $\chi$  pods) to make mixing measurements on oceanographic moorings (Moum and Nash 2009), to which an accompanying fast and local speed measurement adds considerable engineering and scientific value. Specifically, we have developed a technique to measure temperature variance dissipation  $\chi$  on moorings. From a measured time series is derived a frequency spectrum. To convert this to a wavenumber spectrum to which a theoretical spectrum is compared and scaled for quantification of  $\chi$ , a measure of the flow speed past the sensor tip is required. To date, we have relied on ancillary measurements of current speed on the mooring plus  $\chi$  pod-derived estimates of cable motion by integration of measured accelerations (Perlin and Moum 2012). To accomplish the objective of designing a device suitable for deployment on  $\chi$  pods that is capable of measuring both speed and turbulence kinetic energy dissipation rate ( $\varepsilon$ ), we (i) reviewed newly available small, low-power differential pressure sensors; (ii) incorporated a

---

*Corresponding author address:* James Moum, College of Earth, Ocean, and Atmospheric Sciences, Oregon State University, 104 CEOAS Administration Bldg., Corvallis, OR 97331-5503.  
E-mail: moum@coas.oregonstate.edu

common mode rejection scheme to minimize device sensitivity to static pressure, temperature, and acceleration; and (iii) developed calibration procedures to characterize the remaining sensitivity to changes in static pressure, temperature, and acceleration. We then designed a pitot-static tube for use on  $\chi$ pod, and after extensive laboratory and field tests, we have been including these on all recently deployed  $\chi$ pod. While the immediate application, including the demonstration provided herein, is moored measurements, the sensor has potentially broad application to a range of platforms, including gliders, autonomous underwater vehicles (AUVs), towed bodies, and possibly vertical profilers.

Field tests to assess the measurement were made at three sites. Two moorings off Kayak Island, Alaska, were deployed in shallow water (<100 m) in October 2012 as part of a U.S. Naval Research Laboratory breaking surface waves experiment. Each mooring was equipped with a  $\chi$ pod and fully calibrated pitot-static tube (Fig. 1). Nearby acoustic Doppler current profilers (ADCPs) provided independent measures of speed for comparison. Another mooring deployed at 2020-m water depth in Luzon Strait as part of an Office of Naval Research initiative, the Internal Waves in Straits Experiment (IWSE) was outfitted with a  $\chi$ pod and pitot-static tube 20 m above the seafloor in June 2011. This deployment preceded implementation of our common mode rejection scheme and is used here to evaluate the high-frequency (turbulence) part of the measurement, as this deployment was deep and free of surface wave signal. The durations of these experiments were sufficiently long to include multiple high wind events (off Alaska) and several fortnightly spring–neap tidal cycles (IWSE), providing critical dynamic range for evaluation of results.

Herein is described the operating principle (section 2), the basic sensor configuration (section 3), followed by a discussion of wind tunnel tests of the sensors (section 4) plus characterizations of the adverse responses to static pressure, temperature, and acceleration (section 5). Results from two field deployments demonstrate the sensor's capability to measure both mean speeds and, through spectral scaling,  $\varepsilon$  (section 6). A discussion (section 7) and conclusions (section 8) follow the results.

## 2. Principle of operation

A pitot tube is a cylinder with a hemispherical leading edge that contains a pressure port at the stagnation point; this is referred to as the dynamic port. A second port (or ports) along the cylinder behind the leading edge is referred to as the static port. Following Bernoulli's principle, the total pressure at the stagnation point is

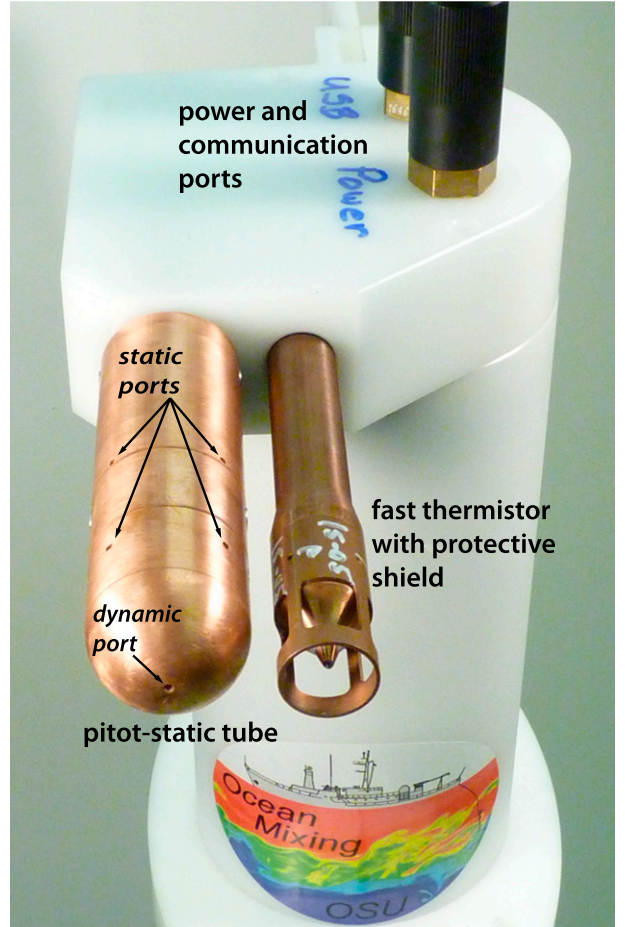


FIG. 1. Pitot-static tube mounted beside fast thermistor on  $\chi$ pod. Each is plugged into a connector in the end cap of the pressure case that houses electronics and batteries. For reference, the visible length of the pitot-static tube extending from the  $\chi$ pod end cap is 10.6 cm. (Photo courtesy of Craig Van Appeldorn.)

$$p = \frac{1}{2}\rho u^2 + p_s, \quad (1)$$

where  $\rho$  is the fluid density,  $u$  is the flow speed—ahead of and perpendicular to—the stagnation point, and  $p$  is the sum of static  $p_s$ , and dynamic ( $1/2\rho u^2$ ) pressures.

A pitot-static (or Prandtl) tube is designed to mechanically isolate the dynamic pressure,

$$p_d = p - p_s = \frac{1}{2}\rho u^2, \quad (2)$$

thus yielding a direct estimate of  $u$  from the measurement of  $p_d$ . This is accomplished by referencing one side of a differential pressure sensor to total pressure and the other side to static pressure, as in the device shown in Fig. 2.

An ideal differential pressure sensor senses only the pressure difference across the device. However, from

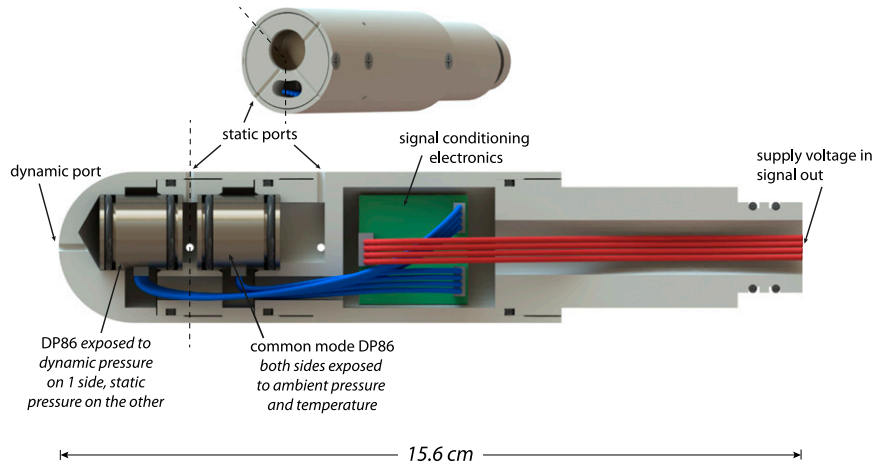


FIG. 2. Cross section of pitot-static tube showing details of the positioning of pitot-static and common mode differential pressure sensors. The cross sections ahead of the signal conditioning electronics are aligned with the dashed lines. The perspective is stylized to provide a clear view of components. (SOLIDWORKS drawing courtesy of Craig Van Appeldorn.)

trials of many sensors over several years, we have found that the responses to static pressure, temperature, and acceleration must also be reduced and characterized. Elimination of these adverse responses is not possible but reduction is attempted by pairing sensors with similar responses to static pressure, temperature, and acceleration in a common mode rejection scheme. Both sensors are exposed to static pressure and temperature through static ports but only one is exposed to total pressure. Both sensors are equally exposed to axial accelerations and to tilting, which changes the gravitational contribution to acceleration in proportion to  $\sin\theta$ , where  $\theta$  is the tilt angle. Common mode rejection of static pressure, temperature, and acceleration is implemented by differencing the output voltages from the two sensors.

The differential pressure sensor is exposed to the dynamic port on one side and static ports on the other. It senses a voltage  $V_r$  that can be represented by

$$V_r = \frac{\partial V_r}{\partial p_d} p_d + \frac{\partial V_r}{\partial p_s} \delta p_s + \frac{\partial V_r}{\partial T} \delta T + \frac{\partial V_r}{\partial a} \delta a + c_r, \quad (3)$$

where the respective derivatives represent sensitivities to  $p_d$ ,  $p_s$ , temperature  $T$ , and acceleration  $a$ . The nominal linear pressure response of the differential pressure transducer is represented by  $(\partial V_r / \partial p_d) p_d$  plus a constant  $c_r$ . Terms  $\delta p_s$ ,  $\delta T$ , and  $\delta a$  represent incremental changes in  $p_s$ ,  $T$ , and  $a$  from a base state, respectively. The definition of the base state is discussed in [section 5d](#).

The second differential pressure sensor (rightmost sensor in [Fig. 2](#)) is exposed to static pressure on both sides and senses a voltage,

$$V_{cm} = \frac{\partial V_{cm}}{\partial p_s} \delta p_s + \frac{\partial V_{cm}}{\partial T} \delta T + \frac{\partial V_{cm}}{\partial a} \delta a + c_{cm}. \quad (4)$$

Internal signal conditioning differences the two voltages,

$$\begin{aligned} V_o &= V_r - V_{cm} \\ &= \frac{\partial V_r}{\partial p_d} p_d + \left( \frac{\partial V_r}{\partial p_s} - \frac{\partial V_{cm}}{\partial p_s} \right) \delta p_s \\ &\quad + \left( \frac{\partial V_r}{\partial T} - \frac{\partial V_{cm}}{\partial T} \right) \delta T + \left( \frac{\partial V_r}{\partial a} - \frac{\partial V_{cm}}{\partial a} \right) \delta a \\ &\quad + c_r - c_{cm}, \end{aligned} \quad (5)$$

or

$$V_o = S_{p_d} p_d + S_{p_s} \delta p_s + S_T \delta T + S_a \delta a + c_o, \quad (6)$$

where

$$\begin{aligned} S_{p_d} &= \frac{\partial V_r}{\partial p_d}, \\ S_{p_s} &= \frac{\partial V_r}{\partial p_s} - \frac{\partial V_{cm}}{\partial p_s}, \\ S_T &= \frac{\partial V_r}{\partial T} - \frac{\partial V_{cm}}{\partial T}, \quad \text{and} \\ S_a &= \frac{\partial V_r}{\partial a} - \frac{\partial V_{cm}}{\partial a} \end{aligned} \quad (7)$$

represent the common mode, or net, sensitivities to  $p_d$ ,  $p_s$ ,  $T$ , and  $a$ , respectively.

Practically,  $p_d$  is computed from the measured voltage as

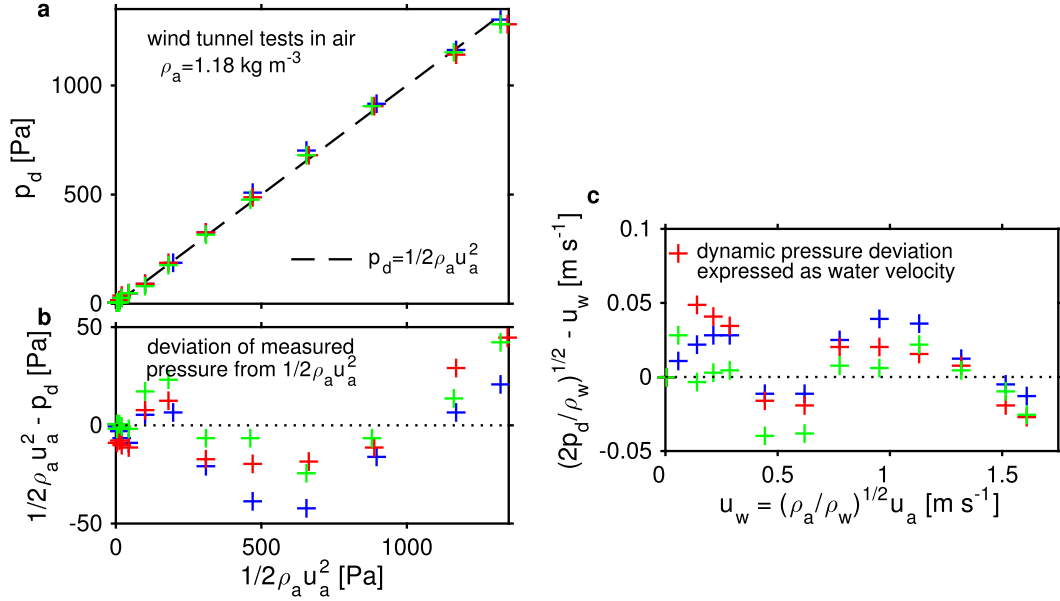


FIG. 3. Wind tunnel tests. These tests were conducted in Oregon State University Mechanical Engineering's Aerolab on three uncompensated pitot-static tubes constructed using DP86L 0–1-psi differential pressure sensors. (a) Comparison of pressure measured by the pitot-static tube to the dynamic pressure estimated independently from wind speed,  $(1/2)\rho_a u_a^2$ ; (b) deviation of measured pitot-static pressure from predicted dynamic pressure; and (c) dynamic pressure deviation in (b) expressed as an equivalent deviation in water speed, plotted vs equivalent water speed.

$$p_d = \frac{1}{S_{p_d}} (V_o - S_{p_s} \delta p_s - S_T \delta T - S_a \delta a - c_o). \quad (8)$$

Individual differential pressure transducers with identical responses to  $p_s$ ,  $T$ , and  $a$  will yield perfect common mode rejection, that is,  $S_{p_s} = 0$ ,  $S_T = 0$ , and  $S_a = 0$ , respectively. This is not achievable in practice and further characterization is required (section 5). Aspects of the practical computation [Eq. (8)] are discussed in section 5d.

### 3. Physical configuration

The basic configuration of the pitot-static tube is shown in Fig. 2. The length, including the O-ring fitted sensor plug, is 15.6 cm. The outside diameter is 3.2 cm. For upper-ocean use, we have built these in copper, as it has proved to be effective at preventing biological fouling in equatorial deployments (Moum and Nash 2009). Using copper, the sensor weight is about 600 g. For higher pressures away from the surface, and because the device itself is a pressure case, we have been using aluminum for construction because of its superior mechanical properties (greater yield strength and lighter weight). Aluminum devices weigh about 200 g.

The differential pressure transducer used here is the DP86L 0–1 psi, manufactured by Measurement Specialties.

This is a piezoresistive silicon pressure sensor in a 316L stainless steel housing that permits direct contact to seawater. We set internal voltage gain and offset to match the expected range of flow speeds plus any static pressure voltage offset induced through  $S_{p_s}$ . Total sensor current draw (including two transducers plus signal conditioning electronics) is 1.5 mA with 5-V supply voltage. For reference, the excitation voltage supplied to the transducers is 4.096 V.

### 4. Wind tunnel tests

Preliminary wind tunnel experiments were done in the Aerolab facility operated by the Mechanical Engineering department on campus. Three pitot-static tubes were built, each with a single uncompensated DP86L sensor and calibrated to determine voltage response as a function of differential pressure applied to the dynamic port using a liquid column manometer. Wind speed ( $u_a$ ) was measured with a Davis Instruments WindScribe ultrasonic sensor mounted in the wind tunnel. Comparisons are shown in Fig. 3.

The difference in the pressure measured by the pitot-static tubes and  $(1/2)\rho_a u_a^2$  ranges from  $-50$  to  $+50$  Pa and is larger than anticipated, which suggests a non-linearity in measurement of either pressure or speed (Fig. 3b). For additional reference, the dynamic pressure



TABLE 1. Sensitivity to static pressure.

Sensitivity to static pressure	(Pa Pa <sub>s</sub> <sup>-1</sup> )	(Pa psi <sup>-1</sup> )	(Pa m <sup>-1</sup> )	[(m s <sup>-1</sup> ) m <sup>-1</sup> ] near 0 m s <sup>-1</sup>	[(m s <sup>-1</sup> ) m <sup>-1</sup> ] near 0.1 m s <sup>-1</sup>
Uncompensated nominal	$8 \times 10^{-5}$	0.6	0.8	0.04	0.002
Compensated nominal	$5 \times 10^{-5}$	0.3	0.5	0.03	0.001
Alaska	$1.5 \times 10^{-5}$	0.1	0.15	0.02	0.0003

deviation is represented as equivalent water speed,  $u_w = \sqrt{\rho_a/\rho_w} u_a$  (Fig. 3c). The sensor's full-scale output is 6900 Pa; a deviation of 50 Pa represents 0.7% of full scale. The manufacturer's specification for the DP86L states the maximum nonlinearity to be 0.3% of full-scale output. The WindScribe specifications state 3% accuracy in speed, or 6% in squared speed. If this is to be taken over full-scale output of  $67 \text{ m s}^{-1}$ , then it represents an inaccuracy of 160 Pa in equivalent dynamic pressure. Hence, the suspicion is that the deviations measured in the wind tunnel are principally due to the measured wind speeds rather than to the dynamic pressures measured by the pitot-static tubes. This point is revisited in section 7.

## 5. Characterization of adverse sensitivities

Tests conducted in our laboratory to characterize the responses of uncompensated DP86L sensors and compensated pitot-static tubes to static pressure, temperature, and acceleration are summarized in Tables 1–3. The responses are measured in volts and, using the measured sensitivity to  $p_d$ , are converted to their relative contribution to dynamic pressure (i.e., Pa Pa<sub>s</sub><sup>-1</sup>, Pa K<sup>-1</sup>, and Pa g<sup>-1</sup>, respectively). Here the unit Pa refers to dynamic pressure and Pa<sub>s</sub> refers to static pressure. Since our concern is the measurement of speed, these are also expressed relative to equivalent speed (e.g., m s<sup>-1</sup> K<sup>-1</sup>). Since  $u^2 = 2p_d/\rho$  [Eq. (2)],  $\delta u = \delta p_d/(\rho u)$ , and the contribution to an error in speed due to an incremental change in equivalent dynamic pressure by a change in temperature, for example, is smaller at greater speed. Hence, the effects are listed in Tables 1–3 at low (near  $0.01 \text{ m s}^{-1}$ ) and moderate (near  $0.1 \text{ m s}^{-1}$ ) speeds. A discussion of the estimation of the quantities listed in Tables 1–3 follows in sections 5a–c.

### a. Properties of the uncompensated DP86L

Tests on three DP86L sensors mounted in our 0–5000-psi pressure vessel showed responses to static pressure ranging from  $-0.5$  to  $-0.8 \text{ Pa m}^{-1}$  of water static pressure head (Pa m<sup>-1</sup> in Table 1). At the nominal analog gain used for the Alaska deployments discussed here ( $245 \text{ Pa V}^{-1}$ , since reduced to  $2700 \text{ Pa V}^{-1}$ ; Fig. 4a), the voltage difference between surface pressure and that at 2000-m water depth is greater than the total voltage range of 4.096 V. Reduced gain was used for the Internal Waves in Straits (IWISE) deployments at 2000 m.

Two-point measurements of fixed-pressure voltage changes to temperature (room temperature and ice bucket) were executed for 104 DP86L sensors and the results are shown in Table 2. Responses ranged from  $-880$  to  $+1100 \text{ Pa K}^{-1}$ , representing a roughly normal distribution about a mean value of  $+70 \text{ Pa K}^{-1}$  with a standard deviation of  $300 \text{ Pa K}^{-1}$ . The difference in sign within the available sample indicates the caution needed in selecting DP86L sensors. The selection of sensors with opposite sign will only make the adverse temperature response worse [according to Eq. (7)].

Two-point measurements of fixed-pressure acceleration response ( $\pm 1 \text{ g}$ ) were done in air for the same 104 DP86L sensors with results shown in Table 3. Responses ranged from  $-4400$  to  $+3300 \text{ Pa g}^{-1}$ . This includes a very few unrepresentative outliers, and 95% of the values ranged from 1500 to  $1650 \text{ Pa g}^{-1}$ .

### b. Properties of the compensated pitot-static tube

A typical set of calibration curves for a single assembled pitot-static tube is shown in Fig. 4. The units correspond to those in Eq. (7); that is,  $S_{p_d}$  has units of  $\text{V Pa}^{-1}$ . These are converted to the units shown in Tables 1–3 using the sensitivity to dynamic pressures in Fig. 4a. The nominal values in Tables 1–3 represent a

TABLE 2. Sensitivity to temperature.

Sensitivity to temperature	(Pa K <sup>-1</sup> )	[(m s <sup>-1</sup> ) K <sup>-1</sup> ] near 0 m s <sup>-1</sup>	[(m s <sup>-1</sup> ) K <sup>-1</sup> ] near 0.1 m s <sup>-1</sup>
Uncompensated nominal	220	0.65	0.35
Compensated nominal	2	0.06	0.004
Alaska	8	0.12	0.017

TABLE 3. Sensitivity to acceleration. Tests done in air.

Sensitivity to acceleration	(Pa g <sup>-1</sup> )	[Pa (5° tilt) <sup>-1</sup> ]	[(m s <sup>-1</sup> ) g <sup>-1</sup> ] near 0.01 m s <sup>-1</sup>	[(m s <sup>-1</sup> ) (5° tilt) <sup>-1</sup> ]	[(m s <sup>-1</sup> ) g <sup>-1</sup> ] near 0.1 m s <sup>-1</sup>	[(m s <sup>-1</sup> ) (5° tilt) <sup>-1</sup> ]
Uncompensated nominal	1500	130	1.7	0.5	1.3	0.06
Compensated nominal	2.3	0.2	0.07	0.02	0.005	0.0004
Alaska	1.2	0.1	0.05	0.014	0.003	0.0002

summary of nine assembled pitot-static tubes and are broadly consistent with Fig. 4. Those specifically measured for the Alaska deployment are listed separately.

The results described in this paper (and on which we have focused present development) were from  $\chi$ pods equipped with pitot-static tubes deployed on moorings.

In this configuration, the final static pressure is fixed, with variations primarily due to tidally varying changes in elevation. However, changes in temperature cannot be predicted and can vary continuously over the course of a deployment. Furthermore, variations in DP86L responses to temperature are large and can have either sign. Consequently, DP86L sensors for these compensated

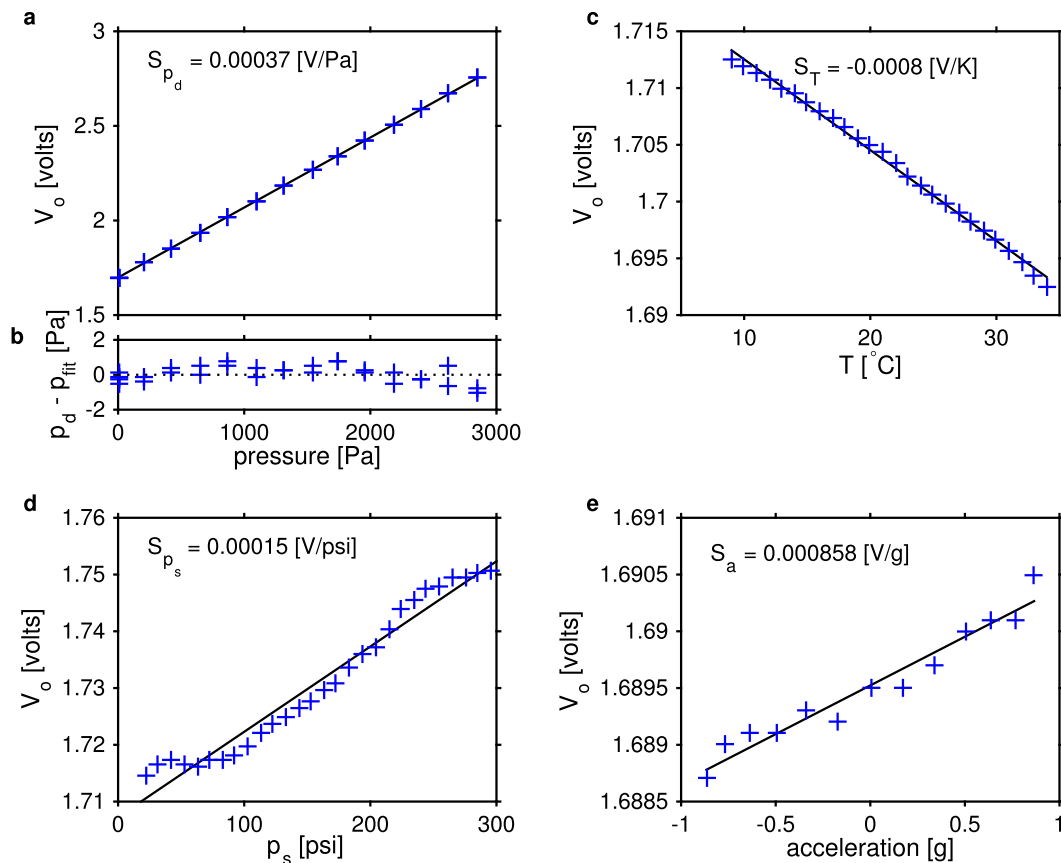


FIG. 4. Typical laboratory calibrations of assembled pitot-static tubes relative to output voltage  $V_o$ . (a) Sensitivity to dynamic pressure, measured using a liquid column manometer. (b) Deviation of measured pressure from the linear fit indicated by the black line in (a). (c) Sensitivity to temperature. (d) Sensitivity to static pressure measured in a nitrogen pressure vessel. (e) Sensitivity to acceleration determined by tilting the sensor relative to its horizontal axis in Fig. 2. The slopes of (a),(c),(d), and (e) were determined by least square fits to the data represented by the blue crosses and indicated as  $S_{p_d}$ ,  $S_T$ ,  $S_{p_s}$ , and  $S_a$ , respectively.

pitot-static tubes were matched with the sole purpose to minimize  $S_T$  in Eq. (7).

The small improvements in static pressure response for the compensated sensors shown in Table 1 are fortuitous, since the DP86L pairs were selected solely for their individual temperature responses. However, they are also relatively small given the expected changes in static pressure at fixed depth. Maximum tidal elevation changes at the 65-m site off Alaska are less than 1 m. The corresponding contamination to speed near  $0.01 \text{ m s}^{-1}$  is less than the speed required to vane the  $\chi$ pod into the flow. At  $0.1 \text{ m s}^{-1}$ , the contamination is  $0.001 \text{ m s}^{-1}$  and smaller at greater speeds.

Matching specifically for temperature response yields a nearly 100-fold reduction in compensated pitot-static tube temperature response (Table 2). With a larger pool of DP86L sensors (not particularly inexpensive) better matching, and hence greater reduction, would be expected. And selection might be made to minimize both temperature and pressure responses. To date, we have simply worked with the number of sensors needed for scheduled deployments.

Reduction in acceleration response is large and due solely to the fact that DP86L responses are so tightly clustered, since this factor was not selected. Table 3 shows the adverse contribution of gravitational acceleration to the measured value of  $p_d$ . Axial accelerations (i.e., accelerations along the axis of the pitot-static tube) also contribute. For guidance, we refer to Fig. 5a in Moum and Nash (2009). This figure shows axial accelerations from  $\chi$ pods deployed on an equatorial mooring with a large surface buoyancy element in a relatively high speed current. Vibrations excited in this situation are at the high end of expected values. Integrating the induced axial accelerations ( $a_x^x$ ) over the higher-frequency band yields an rms acceleration of  $0.05 \text{ g}$ , which contributes an adverse pressure equivalent to a tilt of  $2.5^\circ$ . These vibrations exist outside of the frequency range used to scale the inertial subrange turbulence for estimation of  $\varepsilon$  (section 6b) and do not contaminate that estimate.

The values shown in Tables 1–3 represent *uncorrected* compensated sensitivities. These would represent the contributions to errors in  $p_d$  if we had simply assumed that  $S_p$ ,  $S_T$ , and  $S_a$  were 0 in Eq. (8) and not attempted further correction in postprocessing. For a moored deployment, we would likely consider this to be acceptable in terms of static pressure or acceleration contamination, though perhaps not for temperature response, as temperature changes of many kelvins may be expected in an upper-ocean deployment, for example. We employ the linear fits to these responses to further reduce the error in uniquely interpreting  $p_d$  as dynamic pressure in

Eq. (8) (section 5d). Fortunately,  $S_T$  is reasonably constant over the full range of temperature (Fig. 4b), a small portion to which the sensor would be exposed in a typical moored deployment. The maximum difference (nonlinearity) between measured points and the linear fit of  $V_o$  to  $p_d$  is  $<2 \text{ Pa}$  (Fig. 4b), representing the maximum expected error if use of  $S_T$  perfectly corrects for in situ temperature deviations (section 5d). This represents a fivefold improvement over simply using the compensated pitot-static tube in Fig. 4 over a 5-K temperature range, for example, without taking into account the contribution of  $S_T \delta T / S_{p_d}$ .

### c. Temperature response of $S_{p_d}$

To assess temperature dependence of the sensitivity to differential pressure,  $S_{p_d}$ , calibrations were performed on two compensated pitot-static tubes in the laboratory at two different temperatures, in the early morning at  $13^\circ\text{C}$  and later in the afternoon at  $24^\circ\text{C}$ . These showed differences of  $-0.1\%$  and  $+0.3\%$ , respectively.

### d. Definition of $c_o$

Listed in Fig. 4 are the slopes of each of the curves, determined by linear least squares fitting. Each curve has a nonzero intercept. Calibrations of  $S_{p_d}$  and  $S_{p_s}$  at the natural range of temperatures in our laboratory throughout the day ( $12^\circ$ – $24^\circ\text{C}$ ) indicate no significant change in sensitivities. It is more difficult to do calibrations at different pressures. However, the intercepts do change with changes in temperature. These changes are complicated by the fact that the intercepts are large, out of the calibration range, and that the slopes are linear representations that may not linearly extend to the intercepts. Consequently, there remain small deviations of the no-flow output of the pitot-static tube. We null the output from the field data in postprocessing using the measured no-flow voltage and independently measured pressure, temperature, and acceleration.

The cumulative contribution of the intercepts is denoted  $c_o$  in Eq. (8). For the analysis described here we define  $c_o$  from the observations at a juncture when the mean speed over a 15-min period is at or near  $0 \text{ m s}^{-1}$ . When  $u = 0$ ,  $p_d = 0$ . This is relatively easy to determine in the case of these measurements, as they were accompanied by independent acoustic Doppler measurements of current speed. But the condition also coincides with minimum  $V_o$  [Eq. (8)] as well as fluttering of the  $\chi$ pod as measured by the internal compass when the flow is insufficient to properly vane it. This juncture then defines the reference values of  $p_s$ ,  $T$ , and  $a$ , independently measured at the  $\chi$ pod, from which the deviations— $\delta p_s$ ,  $\delta T$ , and  $\delta a$ , respectively—are defined. Then,



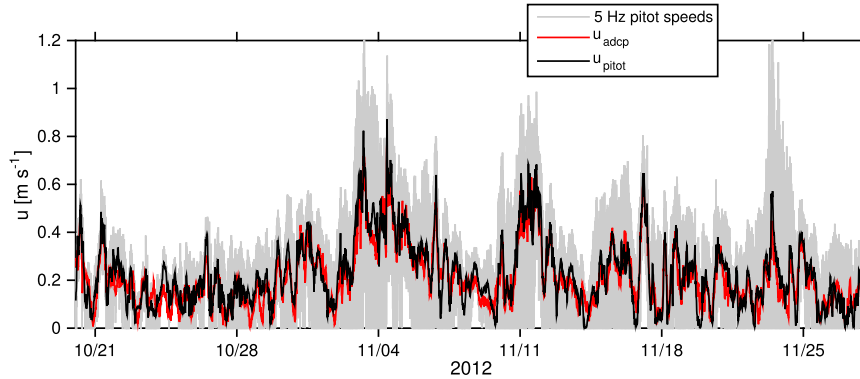


FIG. 5. Time series of speed from a deployment south of Kayak Island in fall 2012. The ADCP was mounted on the seafloor at 65-m depth, 165 m to the east of a string mooring. The string mooring included a  $\chi$ pod similar to that shown in Fig. 1, 8.6 m above the seafloor in 65-m water depth. Pitot-static tube speeds averaged to 0.2-s resolve surface wave orbital velocities. The 15-min averages of speeds are plotted in black and red.

$$c_o = -\frac{V_o}{S_{p_d}} \quad (9)$$

at the reference values.

## 6. Results

To establish the capability of the sensor to measure both  $u$  and  $\varepsilon$ , two different datasets are discussed here. The first, obtained from moorings deployed south of Kayak Island in fall 2012, provides an unambiguous demonstration of the capability of the sensor to measure mean velocity from a simple static pressure calibration and application of measured linear responses to changes in static pressure (here mostly due to the barotropic tide), temperature, and tilting as described in section 5d. However, since this deployment was part of a breaking wave experiment in shallow water and includes a significant wave signal, the inertial subrange of the velocity spectrum, which is governed by turbulence (section 6b), is obscured by the spectral signature of the waves. The second dataset, from 2020-m depth in Luzon Strait obtained in summer 2011 from a mooring with subsurface buoyancy element, highlights the inertial subrange. This latter dataset precedes implementation of our common mode rejection scheme and mean velocities were determined by fitting to independent, acoustically derived speed measurements. As there was no surface wave signal, the inertial subrange is not similarly contaminated by wave signal.

### a. Mean speed

Two moorings deployed south of Kayak Island in late October 2012 were equipped with  $\chi$ Pods roughly 10 m above the seafloor in 65- and 99-m water depth,

respectively. Neither mooring included independent velocity measurements immediately at the site. However, nearby bottom landers included upward-looking ADCPs at respective lateral distances of 165 and 106 m from the moorings. ADCP speed measurements from these landers at roughly the same heights as the pitot-static tubes on the  $\chi$ Pods are used for comparison.

The pitot-static tubes on both  $\chi$ Pods were sampled at 50 Hz. These signals include mean velocities plus surface wave orbital velocities plus turbulence velocities. Averaged to 0.2 s (5 Hz) for simplicity of depiction, peak-to-peak values of wave orbital speeds range from  $O(1 \text{ cm s}^{-1})$  to  $O(10 \text{ cm s}^{-1})$  (gray lines in Fig. 5).

The ADCP data samples are 15-min mean values obtained by ensemble-averaging 90 pings (10 s per ping) at the 65-m depth site and 80 pings (11.125 s per ping) at the 99-m depth site. The ADCP measurements alias the high-frequency signals observed by the pitot-static tube in time while averaging spatial fluctuations over the spread of the four beams. For further comparison, the pitot-static speed estimates were simply averaged to match the sample times of the ADCPs (Fig. 5). The depiction of the fast-sampled speeds in Fig. 5a is misleading, as it emphasizes the extreme speed excursions due to wave orbitals on this time scale. Yet distributions of the three series show strong similarities (Fig. 6). The time series of the two 15-min averaged speeds (Fig. 5) shows the variations over a period during which considerable cooling plus wind forcing combined to completely mix the water column (E. A. Jarowsz et al. 2015, unpublished manuscript). Intense wind events on 2 and 10 November accelerated the full water column; these represent the main mode of variability in the signals in both ADCP and the pitot-static tube, which track each other exceptionally well at all time scales that can be seen in Fig. 5.

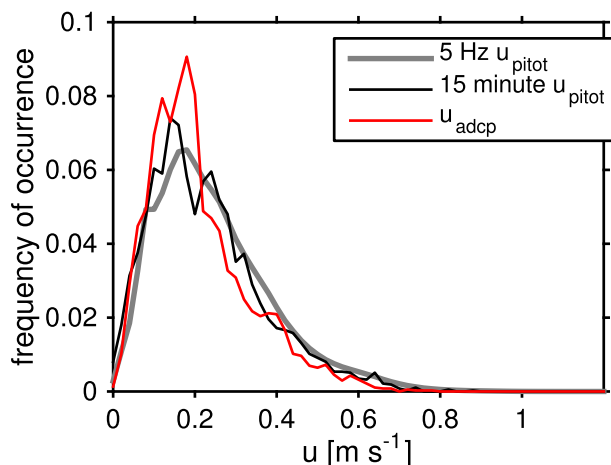


FIG. 6. Histogram of data shown in Fig. 5. Mean values for 5-Hz  $u_{\text{pitot}}$  and 15-min  $u_{\text{pitot}}$  are  $0.23 \text{ m s}^{-1}$  and for  $u_{\text{adcp}}$  is  $0.21 \text{ m s}^{-1}$ .

Direct comparison of  $u_{\text{pitot}}$  and  $u_{\text{adcp}}$  by linear least squares fit shows that the slope of the fit is indistinguishable from 1.0 with 95% confidence (Fig. 7). This is also true for a companion deployment in 99-m water depth (Fig. 8). From these fits, one series has a high bias of  $0.02 \text{ m s}^{-1}$  and the other a low bias of  $0.02 \text{ m s}^{-1}$ .

### b. Turbulence

The shallow-water Alaska deployments include significant surface wave signals that, in the frequency domain, encroach on the inertial subrange of the turbulence. A clearer depiction of the inertial subrange comes from a deployment in Luzon Strait (IWISE mooring N1–20°36'N, 120°51'E) in summer 2011 in 2020-m water depth. The  $\chi$ pod was deployed 20 m from the seafloor above a 300-kHz ADCP. Pitot-static speeds were determined by linear least squares fitting to ADCP speeds at the same depth. While this demonstrated the tendency of the speeds estimated from the measured pressure to track changes in ADCP speed, it did not provide an independent estimate of mean speed. Consequently, these data are only used to demonstrate the estimation of  $\varepsilon$  from the inertial subrange of the velocity spectrum.

A velocity spectrum obtained during a 40-min time period when speed was reasonably steady is shown in Fig. 9. Narrowband spectral peaks at frequencies above 1 Hz correspond to peaks in acceleration spectra (not shown here) and are presumably due to flow-induced cable vibrations. Three lines are shown that fit the measured spectra over the ranges 0.01–0.5, 0.0008–0.05, and 0.0008–0.01 Hz using a  $f^{-5/3}$  slope. Here  $\varepsilon$  is estimated by fitting

$$\Phi_u(k) = A\alpha\varepsilon^{2/3}k^{-5/3} \quad (10)$$

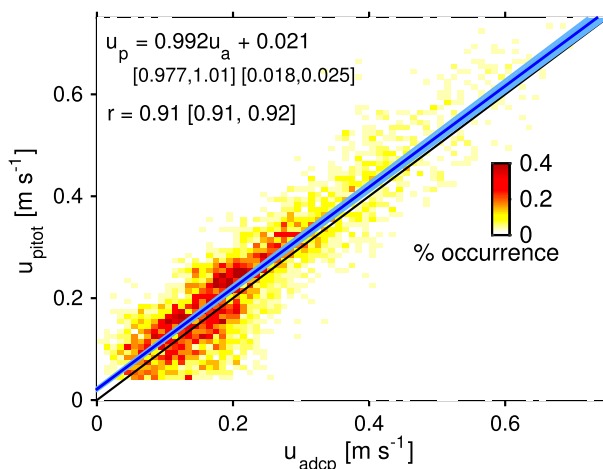


FIG. 7. Comparison of speeds measured by pitot tube and ADCP from the data shown in Fig. 5 depicted as a two-dimensional histogram. The blue line is a linear fit to the data indicated in the top-left corner with 95% confidence limits on the coefficients shown in brackets and by the blue-shaded envelope about the fit. Correlations with 95% confidence limits are denoted by  $r$ . The black line represents  $u_p = u_a$ .

over the ranges indicated above, where  $k = 2\pi f/u$  is the wavenumber component in the direction of the mean speed ( $u$ ),  $\alpha = 1.5$  is Kolmogorov's constant,  $A = 18/55$  represents conversion from a three- to one-dimensional spectrum, and  $\Phi_u(k)$  is the wavenumber spectrum of velocity (e.g., Tennekes and Lumley 1972). Note that the abscissa in Fig. 9 is frequency. The fit to the lowest-frequency range includes inhomogeneity at the lowest frequencies (Peltier et al. 1996) and a small departure from the constant slope at these frequencies.

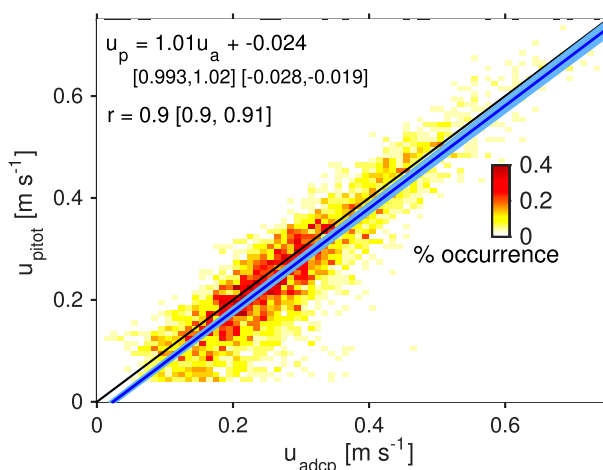


FIG. 8. Comparison of speeds measured by pitot tube and ADCP from another set of measurements farther offshore in 99-m water depth. The separation between ADCP and string mooring was 106 m. Description as in Fig. 7.

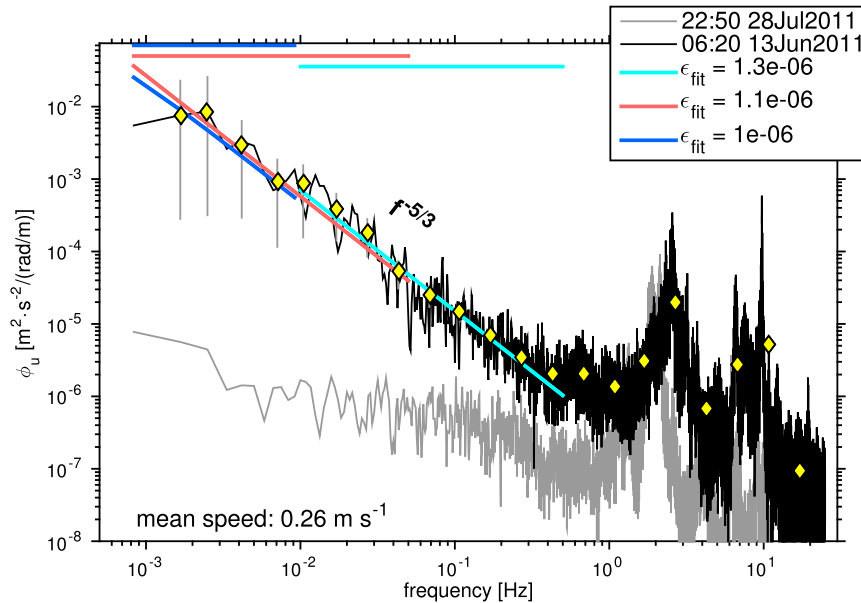


FIG. 9. Spectrum from pitot-static tube mounted on a  $\chi$ pod in 2000-m water depth on a mooring in Luzon Strait on 13 Jun 2011 (black). The spectrum was computed from a 40-min record when the flow speed was relatively constant at  $0.26 \text{ m s}^{-1}$ . Yellow diamonds are logarithmically spaced bin averages. Fits to the inertial subrange portion of the spectrum over frequency ranges denoted by colors yield the estimates of  $\epsilon$  shown in the legend. The gray line represents a spectrum with low signal levels ( $\epsilon < 10^{-9} \text{ m}^2 \text{ s}^{-3}$ ) and a flow speed of  $0.11 \text{ m s}^{-1}$  from 28 Jul 2011.

Despite the disparate frequency ranges, the three estimates of  $\epsilon$  derived from these fits vary only from  $1.0 \times 10^{-6}$  to  $1.3 \times 10^{-6} \text{ m}^2 \text{ s}^{-3}$ . For a frequency of  $0.001 \text{ Hz}$ , the equivalent advected length scale (at  $0.26 \text{ m s}^{-1}$ ) is 260 m. This suggests inhomogeneity of the turbulence compared to predictions from simple boundary layer scaling but is consistent with surface layer measurements in both the atmosphere (Peltier et al. 1996) and the ocean (Wijesekera et al. 2004).

The gray curve in Fig. 9 represents a low-signal-level spectrum for which the inertial subrange is poorly resolved. Estimates of  $\epsilon$  over the frequency ranges shown range from  $10^{-11}$  to  $<10^{-9} \text{ m}^2 \text{ s}^{-3}$ . For now, we should consider the noise level to be at a level  $<10^{-9} \text{ m}^2 \text{ s}^{-3}$ . This spectrum was obtained at a mean speed of  $0.11 \text{ m s}^{-1}$ . The shift in acceleration peaks to a lower frequency is commensurate with cable strumming, roughly defined by a frequency that is linear in velocity,  $f_s = u/5d$ , where  $d$  is the cable's diameter.

Time series derived solely from  $\chi$ pod measurements on the Luzon Strait mooring indicate the predominantly tidal nature of temperature, current speed, and  $\epsilon$  (Figs. 10a–c, respectively), which is typical of this flow regime (Buijsman et al. 2014). Here  $\epsilon$  was not computed where mean speeds are  $<3 \text{ cm s}^{-1}$ , explaining data gaps in Fig. 10c. The mixed diurnal–semidiurnal tides

dominate on the daily time scale, while fortnightly spring–neap variability is clear in all three signals. Despite the fact that  $u$  and  $\epsilon$  are derived from the same measurement, their separation in the frequency domain means that they are functionally independent, aside from errors in calibration of the speed. A scatterplot comparison of daily averaged values (red in Figs. 10b,c), which weights the spring–neap variability, suggests that  $\epsilon$  is roughly proportional to the cubed current speed (Fig. 11).

The motivation for examining the surface wave-free spectra from the deep IWISSE mooring was to isolate the inertial subrange for computation of  $\epsilon$ . The fact that the inertial subrange extends to lower frequencies (or wavenumbers) than we might expect for a homogenous turbulence is leading to a new appreciation of the low wavenumber form of the spectrum in the boundary layer as observed from a fixed platform and provides a means to quantify  $\epsilon$  from an extended inertial subrange that is well separated from surface wave contamination in the frequency domain. Estimates of  $\epsilon$  for the Alaska data are plotted as time series along with surface wind stress, temperature at the  $\chi$ pod, and current speed in Fig. 12. An estimate of the bottom drag coefficient is derived from these estimates following Perlin et al. (2005), where the friction velocity  $u_* = (\epsilon \kappa z)^{1/3}$  is compared to

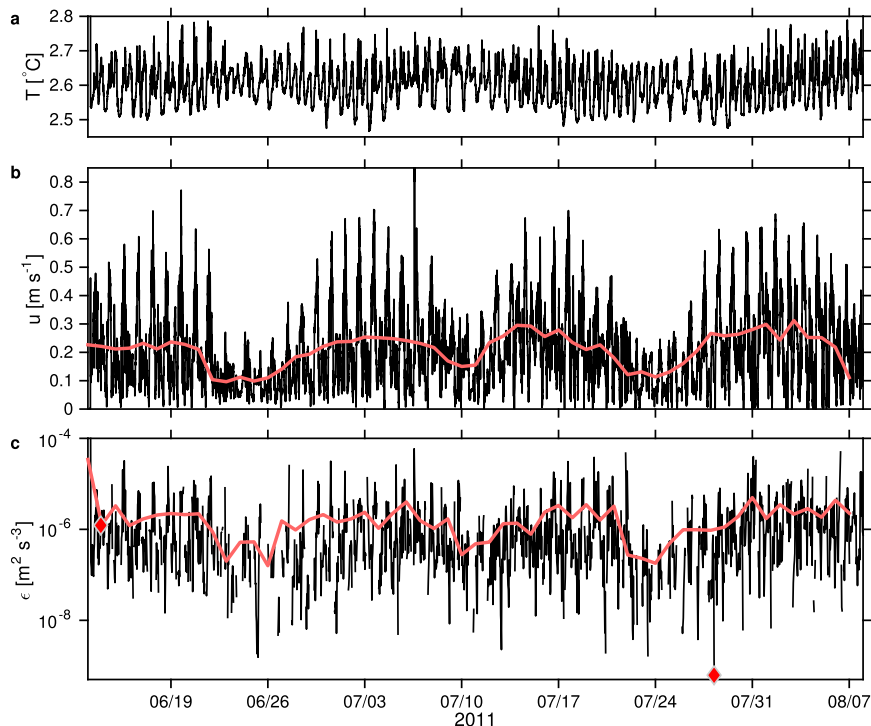


FIG. 10. Time series from a mooring in 2000-m water depth in Luzon Strait in June 2011: (a)  $T$ , (b) current speed (5-min averages), and (c)  $\epsilon$  derived from fits to 40-min time series. The red lines in (b),(c) are daily averages of speed and  $\epsilon$ . The diamonds represent the times and estimated values of  $\epsilon$  for the two spectra shown in Fig. 9.

the speed at 10-m height via the drag coefficient,  $C_D = u_*^2/U_{10}^2$ . Averaged over the duration of the deployment,  $C_D \simeq (1.2 - 1.5) \times 10^{-3}$ , the range representing the values at the two sites. This is comparable to bottom boundary layer estimates derived from profiler measurements using shear probes over Oregon's continental shelf by Perlin et al. (2005).

## 7. Discussion

When we first began using pitot-static tubes, we were concerned that air trapped in the ports would prevent incompressible communication of the pressure to the DP86L sensor. To prevent this, we used a syringe to fill the ports with high-viscosity silicon oil and covered the pitot-static tube with a condom for shipping. However, some oil inevitably dripped out once the condom was removed, creating other problems, such as contaminating the thermistor. Eventually we simply tried deploying the pitot-static tube with no oil and discovered that there was a short period (tens of seconds to minutes) of noisy signal that might be attributed to air bubbles in the ports. This noisy signal soon disappeared, and we have assumed that air bubbles in the ports quickly go into solution under pressure. Resulting signals from the

deployments described here are remarkably clean from mean speeds through to the frequencies of cable vibrations.

While this measurement technique ultimately targets velocity, the evaluation here has focused solely on the basic measurement of speed, which is uncomplicated by

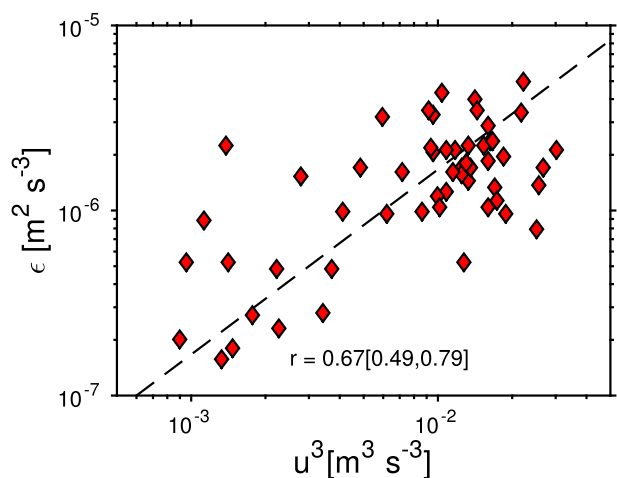


FIG. 11. Scatterplot of daily averaged  $u^3$  vs daily averaged  $\epsilon$  using the data indicated by the red lines in Fig. 10.

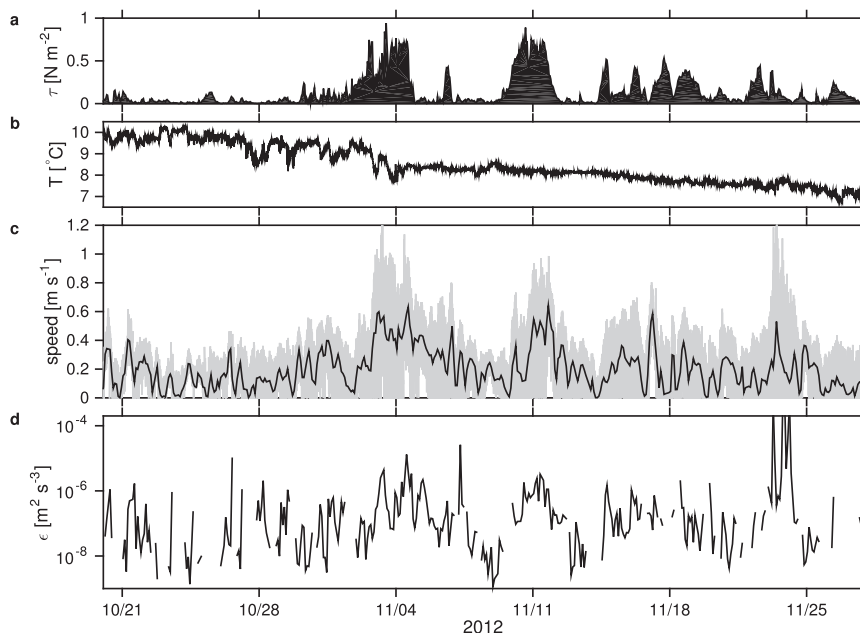


FIG. 12. Time series from the dataset south of Kayak Island in 65-m water depth (Fig. 5): (a) wind stress from a nearby meteorological buoy, (b) temperature, (c) speed as measured by the pitot-static tube, and (d)  $\epsilon$  computed by scaling spectra from 40-min records as in Fig. 9.

the additional assessment of the compass measurement. Reduction of the speed into velocity components using the  $\chi$ pod's internal compass is straightforward. The successful vaning of the  $\chi$ pod into the flow on the equatorial Tropical Atmosphere Ocean (TAO) moorings is discussed by Moum and Nash (2009). The fact that speed measurements  $< 5 \text{ cm s}^{-1}$  are well represented by the pitot-static tubes on  $\chi$ Pods compared to ADCP measurements (in Figs. 5–8) indicates that the vane does an adequate job of steering the sensors into the flow at these low flow speeds, at least on these particular moorings.

The correspondence between the field measurements of speed using pitot-static tubes on two separate moorings with the independent ADCP-derived speeds is encouraging. Comparisons in Figs. 7, 8 show 1:1 agreement, on average, over a large range of oceanic flow speeds. A reasonable explanation for the small bias of  $\pm 0.02 \text{ m s}^{-1}$  is inaccuracy in the estimation of  $c_0$  (section 5d). The root-mean-square error of the residuals (observed minus fitted values) is  $0.055 \text{ m s}^{-1}$  in both cases. This is perhaps not unexpected given the differences in sampling volumes and rates, locations, and averaging between the two measurements. Significantly, the differences are not systematic as would be suggested by the wind tunnel tests (section 4; Fig. 3). This in turn suggests that the nonlinearity in the wind tunnel comparison is due to the flow speed sensor rather than the DP86L differential pressure transducer.

Tables 1–3 can be used to provide rough guidance on DP86L characteristics. Sensitivities to differential pressure are linear to within 0.3% (manufacturer specification) and vary by at most  $\pm 10\%$  between transducers. Sensitivities to acceleration are tightly clustered. We were not able to characterize sensitivities to static pressure for the 104 transducers examined for acceleration and temperature, since at that time we did not have an easy way to do so and these transducers have now been built into pitot-static tubes and deployed on moorings. However, the range of the three sensors we did test was relatively small. Sensitivity to temperature was considerably greater and had both signs. For many applications, such as the moored deployments at fixed static pressure discussed here, matching DP86L sensors so as to maximally reject temperature sensitivity will be the governing consideration, so long as analog voltage gains and offsets keep voltages on scale over the planned deployment pressure (e.g., plus/minus pressure variation due to tides). Our experience shows that this can reduce the temperature sensitivity of the compensated pitot-static tube by nearly a factor of 100. With a sufficiently large pool of DP86L transducers to choose from, one ought to be able to usefully match sensor responses to both static pressure and temperature.

There is no comparative measure of  $\epsilon$  in either of the datasets available for assessment to compare to that derived from the pitot-static speed spectra. This is because estimates of  $\epsilon$  from  $\chi$  (Moum and Nash 2009) are



limited due to the weakly stratified environments of these particular deployments, a point that highlights the complementary benefits of the independent estimate of  $\varepsilon$  provided by the pitot-static tube. What can be said is that the variations in  $\varepsilon$  make sense relative to wind and wave forcing in the Alaska data (Fig. 12) and to the tidally driven flows in Luzon Strait (Fig. 10). Further, there exists a direct correspondence between  $u^3$  and  $\varepsilon$  from the Luzon data (Fig. 11), and drag coefficient estimates based on  $\varepsilon$  and a law of the wall in the bottom boundary layer are consistent with results from similar experiments.

## 8. Conclusions

The device described here

- is physically small and lightweight, making it relatively simple to adapt to existing instrumentation suites or to build new instrumentation using it;
- has low power requirements ( $<10\text{ mW}$ ), enhancing its attractiveness for implementation into other measurement schemes;
- is particularly robust, in comparison to sensors that have been traditionally used for ocean turbulence measurements, such as fast thermistors and shear probes;
- is simply calibrated as static pressure using a liquid column manometer, with ancillary temperature, static pressure, and acceleration calibrations being straightforward;
- provides an independent, fast, and local measure of flow speed (velocity) at the  $\chi$ pod; and
- complements the measurement of  $\chi$  (and derived  $\varepsilon$ ), a factor of particular importance in weakly stratified environments.

Relative to the shear probe, the pitot-static tube provides the full spectrum of velocity not just the dissipation range of the spectrum. This includes mean currents plus linear and nonlinear internal waves, surface waves, and turbulence. Relative to acoustic measurements of velocity, the pitot-static tube requires significantly less power and does not need acoustic scatters in the measurement volume. This makes the sensor a candidate for use in the deep ocean, for example, where signal-to-noise ratios of acoustic sensors are poor.

The critical consideration for implementation is that the pitot-static tube must be aligned with the flow along its axis. Because of the cosine response to the angle of attack, this means a 6% error is introduced at a  $20^\circ$  angle of attack.

One can imagine a multitude of installations where the measure of the complete velocity spectrum from

mean speed through wave orbitals to turbulence will enhance experimental capabilities.

**Acknowledgments.** This work was funded by the Office of Naval Research and the National Science Foundation. Deployments in Alaska were undertaken as part of a U.S. Naval Research Laboratory breaking wave experiment led by David Wang, Hemantha Wijesekera, and Ewa Jarowsz. Deployments in Luzon Strait by Matthew Alford and John Mickett were part of ONR's Internal Waves in Straits Experiment (IWISE). I am grateful to all of the above-mentioned organizations and individuals for these deployments and for sharing ADCP data to compare to these pitot-static speed measurements. The  $\chi$  pods were constructed by Ray Kreth. Mark Borgerson contributed fundamentally to development of the pitot-static tubes, including the calibration procedures and the wind tunnel tests. Mike Neeley-Brown built thermistors and helped with logistics and construction. Alexander Perlin participated in recovery of the Alaska moorings, downloaded the  $\chi$ pod data, and made a low-level analysis while at sea. Many thanks to Jim Liburdy for arranging our use of the Aerolab wind tunnel in Mechanical Engineering. Craig Van Appeldorn, Pavan Vutukur, and Rex Nelson contributed in various ways. Bill Smyth, Emily Shroyer, Sally Warner, Aurelie Moulin, and Martin Hoecker-Martinez made helpful comments on an early draft of this manuscript. Further suggestions by two anonymous reviewers resulted in significant improvement to the final submission compared to the first.

## REFERENCES

- Buijsman, M. C., and Coauthors, 2014: Three-dimensional double-ridge internal tide resonance in Luzon Strait. *J. Phys. Oceanogr.*, **44**, 850–869, doi:[10.1175/JPO-D-13-024.1](https://doi.org/10.1175/JPO-D-13-024.1).
- Moum, J. N., 1990a: Profiler measurements of vertical velocity fluctuations in the ocean. *J. Atmos. Oceanic Technol.*, **7**, 323–333, doi:[10.1175/1520-0426\(1990\)007<0323:PMOVVF>2.0.CO;2](https://doi.org/10.1175/1520-0426(1990)007<0323:PMOVVF>2.0.CO;2).
- , 1990b: The quest for  $K_p$ —Preliminary results from direct measurements of turbulent fluxes in the ocean. *J. Phys. Oceanogr.*, **20**, 1980–1984, doi:[10.1175/1520-0485\(1990\)020<1980:TQFRFD>2.0.CO;2](https://doi.org/10.1175/1520-0485(1990)020<1980:TQFRFD>2.0.CO;2).
- , 1996a: Efficiency of mixing in the main thermocline. *J. Geophys. Res.*, **101**, 12 057–12 069, doi:[10.1029/96JC00508](https://doi.org/10.1029/96JC00508).
- , 1996b: Energy-containing scales of turbulence in the ocean thermocline. *J. Geophys. Res.*, **101**, 14 095–14 109, doi:[10.1029/96JC00507](https://doi.org/10.1029/96JC00507).
- , and J. D. Nash, 2009: Mixing measurements on an equatorial ocean mooring. *J. Atmos. Oceanic Technol.*, **26**, 317–336, doi:[10.1175/2008JTECHO617.1](https://doi.org/10.1175/2008JTECHO617.1).
- Peltier, L. J., J. C. Wyngaard, S. Khanna, and J. G. Brasseur, 1996: Spectra in the unstable surface layer. *J. Atmos.*

- Sci.*, **53**, 49–61, doi:[10.1175/1520-0469\(1996\)053<0049:SITUSL>2.0.CO;2](https://doi.org/10.1175/1520-0469(1996)053<0049:SITUSL>2.0.CO;2).
- Perlin, A., and J. N. Moum, 2012: Comparison of thermal variance dissipation rates from moored and profiling instruments at the equator. *J. Atmos. Oceanic Technol.*, **29**, 1347–1362, doi:[10.1175/JTECH-D-12-00019.1](https://doi.org/10.1175/JTECH-D-12-00019.1).
- , —, J. M. Klymak, M. D. Levine, T. Boyd, and P. M. Kosro, 2005: A modified law-of-the-wall applied to oceanic bottom boundary layers. *J. Geophys. Res.*, **110**, C10S10, doi:[10.1029/2004JC002310](https://doi.org/10.1029/2004JC002310).
- Tennekes, H., and J. L. Lumley, 1972: *A First Course in Turbulence*. MIT Press, 300 pp.
- Wijesekera, H. W., C. A. Paulson, and E. D. Skylingstad, 2004: Scaled temperature spectrum in the unstable oceanic surface layer. *J. Geophys. Res.*, **109**, C03015, doi:[10.1029/2003JC002066](https://doi.org/10.1029/2003JC002066).